Frequency selection mechanisms in the flow of a laminar boundary layer over a shallow cavity

Ubaid Ali Qadri and Peter J. Schmid
Department of Mathematics, Imperial College London, London SW7 2AZ, United Kingdom
(Received 2 March 2016; published 10 January 2017)

We investigate the flow over shallow cavities as a representative configuration for modeling small surface irregularities in wall-bounded shear flows. Due to the globally stable nature of the flow, we perform a frequency response analysis, which shows a significant potential for the amplification of disturbance kinetic energy by harmonic forcing within a certain frequency band. Shorter and more shallow cavities exhibit less amplified responses, while energy from the base flow can be extracted predominantly from forcing that impacts the cavity head on. A structural sensitivity analysis, combined with a componentwise decomposition of the sensitivity tensor, reveals the regions of the flow that act most effectively as amplifiers. We find that the flow inside the cavity plays a negligible role, whereas boundary layer modifications immediately upstream and downstream of the cavity edges contribute significantly to the frequency response. The same regions constitute preferred locations for implementing active or passive control strategies to manipulate the frequency response of the flow.

DOI: 10.1103/PhysRevFluids.2.013902

I. INTRODUCTION

Under realistic conditions, surfaces on air, marine, or ground transportation vehicles are subject to imperfections that manifest themselves as gaps, steps, bumps, dips, or other localized irregularities. These geometric features are often the consequence of the manufacturing process or the result of accidental damage or operational fatigue. These surface modifications lead to a rise of roughness-induced flow responses that can take the form of a shift in preferred frequencies or the triggering of instabilities.

While surface irregularities are unavoidable under realistic circumstances, a successful design should exhibit a reasonable degree of robustness to such geometric deformities. It is important then to study their influence on the stability and response of common flow configurations and extract the mechanisms that modify the flow behavior. A study of this kind will also form a basis for control efforts, which would aim to counteract the effect of surface irregularities and reduce their influence to a minimally disruptive level.

In general, surface irregularities, such as bumps, steps, and gaps, cause the boundary layer developing over a surface to separate. The separated shear layer may then reattach further downstream, leading to a region of recirculating fluid, known as a separation or recirculation bubble. A flow with a separation bubble first becomes globally unstable to a steady or low-frequency spanwise-periodic three-dimensional mode [1,2]. This has been found to be true in a variety of flow configurations. As a generic flow configuration, representative of a range of surface irregularities, we consider the flow over an open shallow cavity. This type of flow captures many of the features and amplification processes that are present in other configurations. Consequently, the analysis framework that is presented here carries over in a straightforward manner to other flow configurations.

Numerous studies have investigated the effect of cavity geometry, compressibility, and incoming boundary layer thickness on the three-dimensional instability in the flow over an open cavity [3–5]. The global instability arises from a centrifugal instability mechanism [3] involving the recirculating flow inside the cavity [6]. In these previous studies, the boundary layer thickness upstream of the cavity is an order of magnitude (or more) smaller than the depth of the cavity, and increasing the boundary layer thickness has a stabilizing effect on the instability.

In this paper, we study the case where the boundary layer thickness is of the same order of magnitude as the depth of the cavity. We refer to this flow configuration as a shallow cavity. In contrast to previous studies on open cavity flows, the flow is globally stable and behaves as a hydrodynamic amplifier. In other words, the flow experiences oscillations only in the presence of external forcing or noise and amplifies these disturbances selectively. The unsteadiness arises from a superposition of all linear global eigenmodes with negative growth rates. For the flow over a shallow cavity, the linear dynamics of the flow are thus more appropriately represented by its response to external forcing [7]. This response is quantified by calculating the optimal frequency response (or transfer function) curve and identifying the forcing structure that is linearly most amplified for a given frequency. This amplification occurs in the absence of any unstable eigenmodes due to the non-normality of the linear operator that governs the perturbation dynamics [8,9]. This approach has been applied to other flow configurations that behave as amplifiers, such as, e.g., a flat plate boundary layer [10,11], a laminar separation bubble induced by an adverse pressure gradient [12], a separated boundary-layer flow past a bump [13], the flow behind a rounded backward-facing step [14], a uniform-density axisymmetric jet [15], and the flow induced by radial wall injection [16]. It has been found to successfully predict the frequencies as well as the spatial structures that dominate the dynamics of the flow.

In Sec. II, we describe the flow configuration and give details of the numerical discretization. In Sec. III, we present the mathematical formulation and numerical techniques to calculate the optimal frequency response. In contrast to most previous studies, we consider both two-dimensional and periodic three-dimensional forcing. We identify the frequency and spatial structure of the forcing that yields the most amplified response and investigate the effect of cavity geometry on the optimal gain. Finally, in Sec. IV, we investigate the physical mechanisms that drive and determine the optimal response; in particular, we assess the impact of the flow within the cavity and its vicinity on the linear response characteristics. Concluding remarks are presented in Sec. V. An Appendix gives details on a numerical convergence study.

II. FLOW CONFIGURATION

We consider the motion of a viscous, incompressible fluid over a rectangular, shallow cavity in a domain, Ω, as shown in Fig. 1. The fluid is described by its state vector, $\mathbf{q} = (\mathbf{u}, p)^T$, which contains the pressure p and velocity $\mathbf{u} = (u_x, u_y, u_z)^T$ in the streamwise (x), cross-stream (y), and spanwise (z) directions, respectively. The incoming flow at $x = X_{\min}$ is prescribed by the Blasius velocity profile. The flow variables, cavity length L, and cavity depth D, are made nondimensional using the free-stream velocity, U_∞, and the 99% boundary-layer thickness, δ, at the inlet.

The motion of the fluid is governed by the incompressible Navier-Stokes (NS) equations in nondimensional form, given as

$$\nabla \cdot \mathbf{u} = 0, \quad \frac{\partial \mathbf{u}}{\partial t} + \mathbf{u} \cdot \nabla \mathbf{u} + \nabla p - \frac{1}{\mathrm{Re}} \nabla^2 \mathbf{u} = 0, \tag{1}$$

where the Reynolds number, Re, is defined in terms of U_∞ and δ.

Upon assuming that the incoming flow is spanwise independent, we seek a steady two-dimensional solution to (1). The governing equations are recast in a weak formulation and discretized on the computational domain shown in Fig. 1(a) using the finite-element method. We use Taylor-Hood elements for the velocity (P2) and pressure (P1) fields. No-slip Dirichlet condition for the velocities are imposed along the wall, $\mathbf{u} = \mathbf{0}$, while viscous stress-free boundary conditions, $-p\mathbf{n} + \mathrm{Re}^{-1} \nabla \mathbf{u} \cdot \mathbf{n} = \mathbf{0}$ are applied at the outlet ($x = X_{\max}$) and along the top boundary ($y = Y_{\max}$).

Figure 1(a) shows the steady base flow obtained in a computational domain with $X_{\min} = -20.0$, $X_{\max} = 27.5$, and $Y_{\max} = 5.0$, for a cavity with dimensions $L = 5, D = 1$ at a Reynolds number of

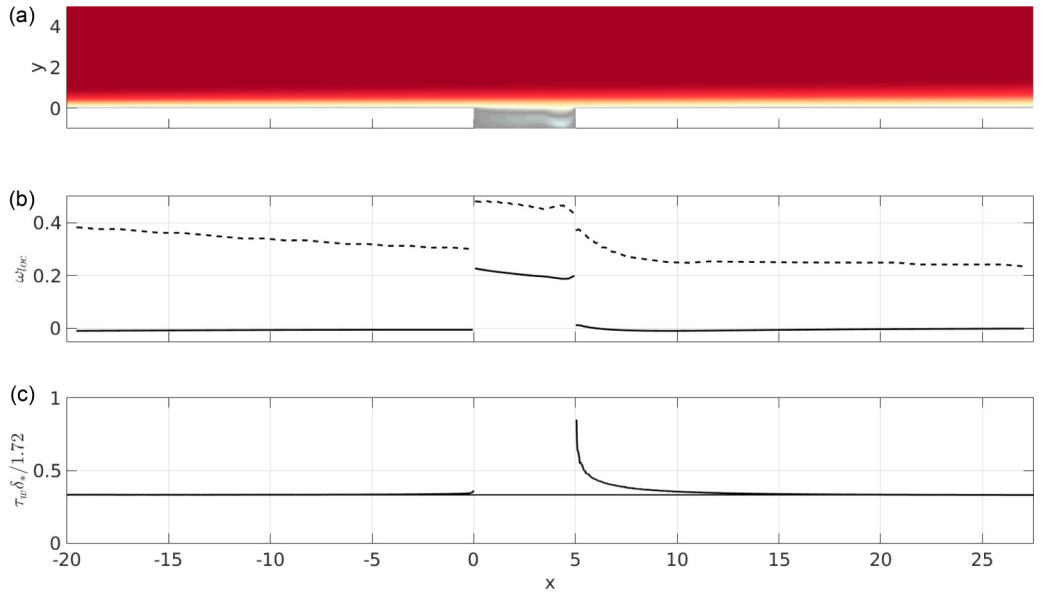

FIG. 1. Flow configuration. (a) Contours of the streamwise velocity for the steady flow over a shallow cavity with $L = 5, D = 1$ at $\mathrm{Re} = 1000$. (b) The local temporal growth rate $\mathrm{Im}(\omega_{\mathrm{loc}})$ (solid), and frequency $\mathrm{Re}(\omega_{\mathrm{loc}})$ (dashed) for the base flow above. (c) The wall shear coefficient for the base flow above. The thick black line corresponds to the value for a Blasius boundary layer.

$\mathrm{Re} = 1000$. This corresponds to an inlet Reynolds number based on the displacement thickness of $\mathrm{Re}_{\delta^*} = 350$, which falls well below the threshold at which a Blasius boundary layer becomes locally unstable ($\mathrm{Re}_{\delta^*} = 519$).

The domain size is motivated by our interest in the amplification properties of the cavity, rather than the amplification properties of the boundary layer. The inlet X_{min} and outlet X_{max} are placed sufficiently far from the upstream and downstream edges of the cavity. In addition, the value of X_{max} has been chosen such that the boundary layer at the outlet is locally stable. The top boundary Y_{max} has been placed sufficiently far from the wall to allow the spatial structures of the forcing and response to be fully captured within the domain. We have validated the convergence of the frequency response with respect to domain size and spatial resolution; results of this study are presented in Appendix.

The cavity depth is of the order of the boundary layer thickness, which is rather shallow compared to previous studies on the flow over open cavities. The maximum reverse flow in the cavity is only about 8%, and we find, using local stability analysis, that the flow is not locally absolutely unstable anywhere within the domain. This agrees with a trend found in a previous study [17] that suggested that the maximum reverse flow in a laminar separation bubble would need to be larger than 12% for absolute instabilities to arise. The flow is, however, convectively unstable between $0 < x < 6.1$. The local temporal growth rate and frequency, calculated by interpolating the local flow profile onto a Gauss-Lobatto grid with 100 points, are shown in Fig. 1(b).

In Fig. 1(c), we plot the local wall-shear coefficient and compare it to the value for a Blasius boundary layer ($f''(0) = 0.332$, with f denoting the Blasius similarity solution). As expected, the boundary layer upstream and downstream of the cavity is influenced by the adverse pressure gradient brought about by the cavity. The presence of the cavity leads to an increase in the wall-shear stress. It is interesting to note, however, that the influence upstream of the cavity is markedly less than the effect downstream of the cavity.

III. RESPONSE TO HARMONIC FORCING

A. Formulation

We are interested in the response of the flow in Fig. 1 to small-amplitude external forcing. We model this forcing as a body force, $\mathbf{f}(\mathbf{x},t)$ acting on the momentum equation in (1). Assuming that the forcing amplitude is small, the dynamics of the flow response are governed by the forced linearized Navier-Stokes equations

$$\nabla \cdot \mathbf{u}' = 0, \quad \frac{\partial \mathbf{u}'}{\partial t} + \mathbf{u}' \cdot \nabla \bar{\mathbf{u}} + \bar{\mathbf{u}} \cdot \nabla \mathbf{u}' + \nabla p' - \frac{1}{\mathrm{Re}} \nabla^2 \mathbf{u}' = \psi(\mathbf{x}) \mathbf{f}', \tag{2}$$

where $\psi(\mathbf{x})$ has been introduced to restrict the forcing to a particular region in the computational domain. In the above expression, the $'$ denotes perturbation quantities, while $\bar{}$ represents steady base-flow variables.

Within the linear framework, we assume that the forcing can be decomposed into a sum of independent Fourier modes in time and in the spanwise direction. The forcing thus takes on the form $\mathbf{f}'(\mathbf{x},t) = \hat{\mathbf{f}}(x,y)e^{\mathrm{i}(kz+\omega t)}$, with ω as the forcing frequency and k as the spanwise wave number, and the perturbation state vector $\mathbf{q}'$ asymptotically responds in kind, i.e., $\mathbf{q}'(\mathbf{x},t) = \hat{\mathbf{q}}(x,y)e^{\mathrm{i}(kz+\omega t)}$.

We discretize the equations using the above-mentioned finite-element method on the same mesh as the one used to obtain the base flow in Fig. 1. At the inlet, along the wall, and on the top boundary, we impose homogeneous no-slip Dirichlet conditions for the velocity, $\hat{\mathbf{u}} = \mathbf{0}$. At the outlet ($x = X_{\max}$), we apply a viscous stress-free boundary condition, $-\hat{p}\mathbf{n} + \mathrm{Re}^{-1} \nabla \hat{\mathbf{u}} \cdot \mathbf{n} = \mathbf{0}$. The discrete linear system can then be rewritten in the form

$$(\mathbf{L} + \mathrm{i}\omega \mathbf{B})\hat{\mathbf{q}} = \mathbf{B_f} \mathbf{P} \hat{\mathbf{f}}, \tag{3}$$

where $\mathbf{L}$ and $\mathbf{B}$ are sparse matrices representing the Navier-Stokes equations in the frequency domain, $\mathbf{B_f}$ applies a selected spatial restriction on the forcing, and $\mathbf{P}$ denotes a prolongation matrix from the velocity space to the velocity-pressure space, $\hat{\mathbf{q}} = \mathbf{P}\hat{\mathbf{u}}$.

We are interested in finding the forcing that is most amplified by the flow. To this end, we measure the amplitude of the forcing and the response using respective L^2 norms, which can be expressed in terms of the inner products $\langle \hat{\mathbf{f}}, \hat{\mathbf{f}} \rangle = \hat{\mathbf{f}}^H \mathbf{Q_f} \hat{\mathbf{f}} \equiv \int_\Omega \hat{\mathbf{f}}^H \hat{\mathbf{f}} \, dV$, and $\langle \hat{\mathbf{q}}, \hat{\mathbf{q}} \rangle = \hat{\mathbf{q}}^H \mathbf{Q} \hat{\mathbf{q}} \equiv \int_\Omega \hat{\mathbf{u}}^H \hat{\mathbf{u}} \, dV$, where $\mathbf{Q_f} = \mathbf{P}^T \mathbf{Q} \mathbf{P}$ and $\mathbf{Q}$ is defined to produce the Euclidean norm of the velocity in the full state-vector over the entire computational domain.

For a particular value of the frequency ω and spanwise wave number k, and a prescribed forcing distribution, the amplification is given by the energy gain $G^2(k,\omega,\hat{\mathbf{f}}) = \langle \hat{\mathbf{q}}, \hat{\mathbf{q}} \rangle / \langle \hat{\mathbf{f}}, \hat{\mathbf{f}} \rangle$. The maximum possible amplification is obtained by maximizing this gain over all possible forcing structures. The discrete optimization problem reads

$$G^2(k,\omega) = \max_{\hat{\mathbf{f}}} \frac{\hat{\mathbf{q}}^H \mathbf{Q} \hat{\mathbf{q}}}{\hat{\mathbf{f}}^H \mathbf{Q_f} \hat{\mathbf{f}}} = \max_{\hat{\mathbf{f}}} \frac{\hat{\mathbf{f}}^H \mathbf{R}^H \mathbf{Q} \mathbf{R} \hat{\mathbf{f}}}{\hat{\mathbf{f}}^H \mathbf{Q_f} \hat{\mathbf{f}}}, \tag{4}$$

where $\mathbf{R}(k,\omega) \equiv (\mathbf{L} + \mathrm{i}\omega \mathbf{B})^{-1} \mathbf{B_f} \mathbf{P}$ is referred to as the discrete resolvent operator.

Formally, the solution to this problem can be obtained by calculating the singular value decomposition (SVD) of $\mathbf{R}$. The leading singular value, G_o, identifies the optimal forcing $\hat{\mathbf{f}}_\mathbf{o}$ that leads to the optimal response $\hat{\mathbf{q}}_\mathbf{o}$. Specifically, the optimal forcing is given by the principal right singular vector, while the optimal response follows from the principal left singular vector.

Since we are only interested in the largest singular mode, a different approach is taken here. Instead of calculating the SVD, we solve the optimization problem (4) by using the Rayleigh quotient and recasting it as a Hermitian eigenvalue problem of the form

$$\mathbf{Q_f^{-1}} \mathbf{R^H} \mathbf{Q} \mathbf{R} \hat{\mathbf{f}} = G^2 \hat{\mathbf{f}}. \tag{5}$$

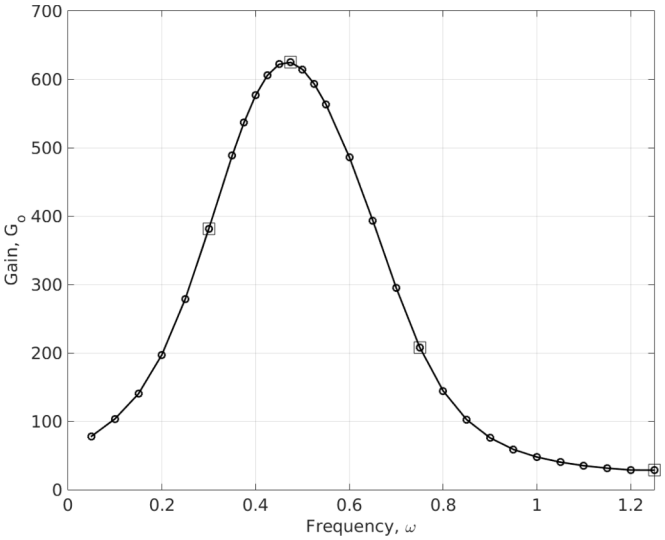

FIG. 2. Optimal gain curve $G_o(0,\omega)$ for two-dimensional forcing.

We generate the large sparse matrices, $\mathbf{L}$,$\mathbf{B}$,$\mathbf{Q}$, and $\mathbf{B_f}$ using FreeFem++, and solve the eigenvalue problem (5) in MATLAB using the Arnoldi-Krylov subspace method. In addition, we perform the matrix inverses using sparse LU decompositions. The leading eigenvalue and eigenvector respectively produce the optimal gain $G_o(k,\omega)$ and the optimal forcing $\hat{\mathbf{f}}_o(k,\omega)$. The corresponding optimal response $\hat{\mathbf{q}}_o(k,\omega)$ is straightforwardly calculated using (3).

B. Response to two-dimensional forcing

We first set $k = 0$ and consider the response to purely two-dimensional forcing. Figure 2 shows the optimal gain curve obtained. The maximum gain, $G_{\max}|_{k=0} = 625$ is obtained for a frequency of $\omega_{\max}|_{k=0} = 0.465$, and Fig. 3 shows the associated optimal forcing and response for a selection of frequencies. The optimal forcing for $\omega = 0.465$ is located in the boundary layer upstream of the cavity and consists of flow structures that are tilted against the mean shear. It has largest magnitude

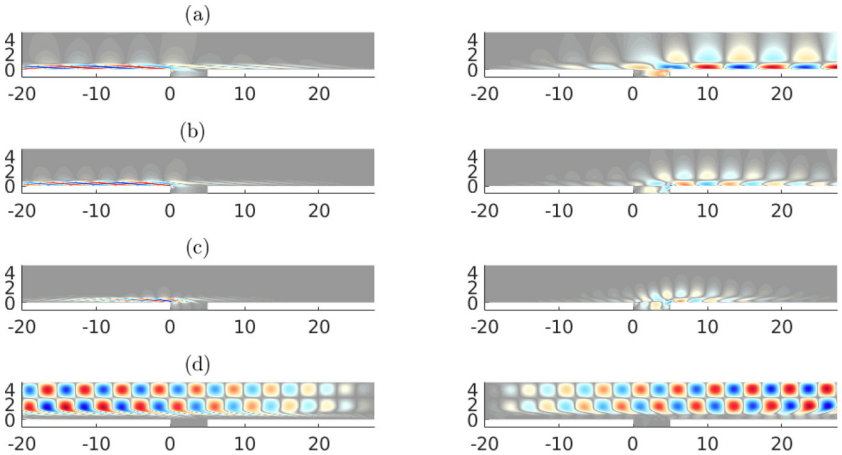

FIG. 3. The real component of the streamwise velocity of the optimal forcing (left) and response (right) for a range of frequencies for two-dimensional forcing. (a) $\omega = 0.30$, (b) $\omega = 0.465$, (c) $\omega = 0.75$, and (d) $\omega = 1.25$.

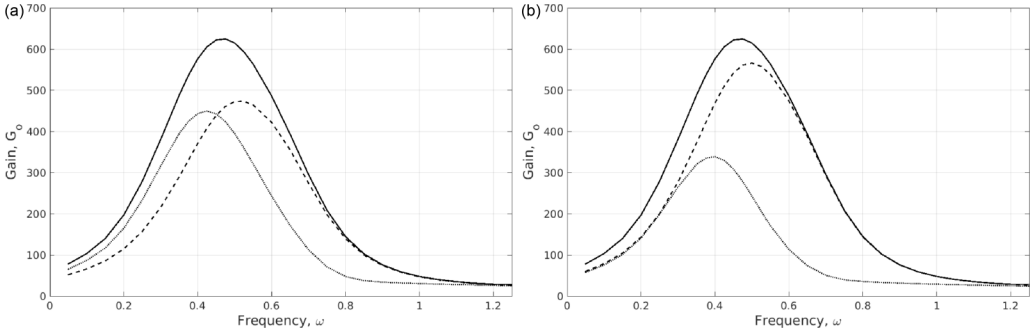

FIG. 4. The optimal gain curves obtained by applying a masking function to compare the contribution of the region $x < X_m$ (dashed) and $x > X_m$ (dotted) to the overall gain (solid) for (a) $X_m = 10.0$ and (b) $X_m = 15.0$ for a cavity with $L = 5$ and $D = 1$ at $\mathrm{Re} = 1000$.

near the upstream edge of the cavity. This corresponds to the locally convectively stable/unstable boundary. The most amplified global frequency is also close to the frequency of the most unstable local mode at this location.

The optimal response has largest magnitude near the downstream edge of the cavity and develops into the boundary layer downstream. This corresponds to the locally convectively unstable/stable boundary. Its spatial structure is very similar to that observed for Tollmien-Schlichting (TS) waves in previous studies [10,13]. This finding highlights and confirms the importance of the inviscid Orr mechanism in the nonmodal amplification of disturbances in the flow. In previous studies [13,14] where the incoming boundary layer was relatively thin with respect to the cavity depth, the optimal forcing that exploits the Orr mechanism was found to be localized near the separation point. In contrast, in this study, the Orr mechanism remains important some distance upstream of the cavity. We expect this to be true for flow over other geometries where the boundary layer thickness is of the same order as the height of the surface irregularity.

At lower frequencies, $0.2 < \omega < 0.465$, Fig. 3(a) shows that the spatial shape of the optimal structures is similar, but the optimal forcing and response have longer wavelengths and extend over a larger distance upstream and downstream of the cavity. The amplitude gain of these structures (in our case, for $\omega = 0.3$) is markedly lower though. At higher frequencies, $0.465 < \omega < 1.25$, Fig. 3(c) shows that the optimal forcing and response have shorter wavelengths and are more localized towards the upstream and downstream edge of the cavity, respectively. At even higher frequencies, $\omega \geqslant 1.25$, Fig. 3(d) shows that the optimal forcing and response correspond to the amplification of vortical free-stream disturbances by the convective nature of the flow. Similar structures have been observed in previous studies [14,15] and are associated with the continuous spectrum of $\mathbf{L}$.

We can identify the contribution of different regions of the flow to the amplification (gain) by applying a masking function to the norm matrix $\mathbf{Q}$. We employ this technique to compare the contribution of the cavity with the contribution of the boundary layer further downstream. The contribution of the downstream boundary layer is found using the Heaviside step function $H(x - X_m)$, where X_m is some streamwise location downstream of the cavity. The contribution of the cavity is found using $-H(x - X_m)$. Figure 4 shows the optimal gain curves obtained for $X_m = 10.0$ and $X_m = 15.0$. In both cases, we find that the region with the cavity preferentially selects a higher frequency than the region with the boundary layer downstream. Comparing the contribution of the cavity to the overall gain, we find that the optimal gain for $X_m = 10.0$ amounts to 75% of the optimal gain for the full domain. For $X_m = 15.0$, this rises to 90%. This observation highlights the dominant role of the cavity and the boundary layer immediately downstream in the frequency selection mechanism.

C. Response to spanwise-periodic three-dimensional forcing

We now set $k > 0$ and consider the response of the flow to three-dimensional but spanwise-periodic harmonic forcing. Figure 5(a) reports how the maximum gain $G_{\max}(k)$ and the frequency at

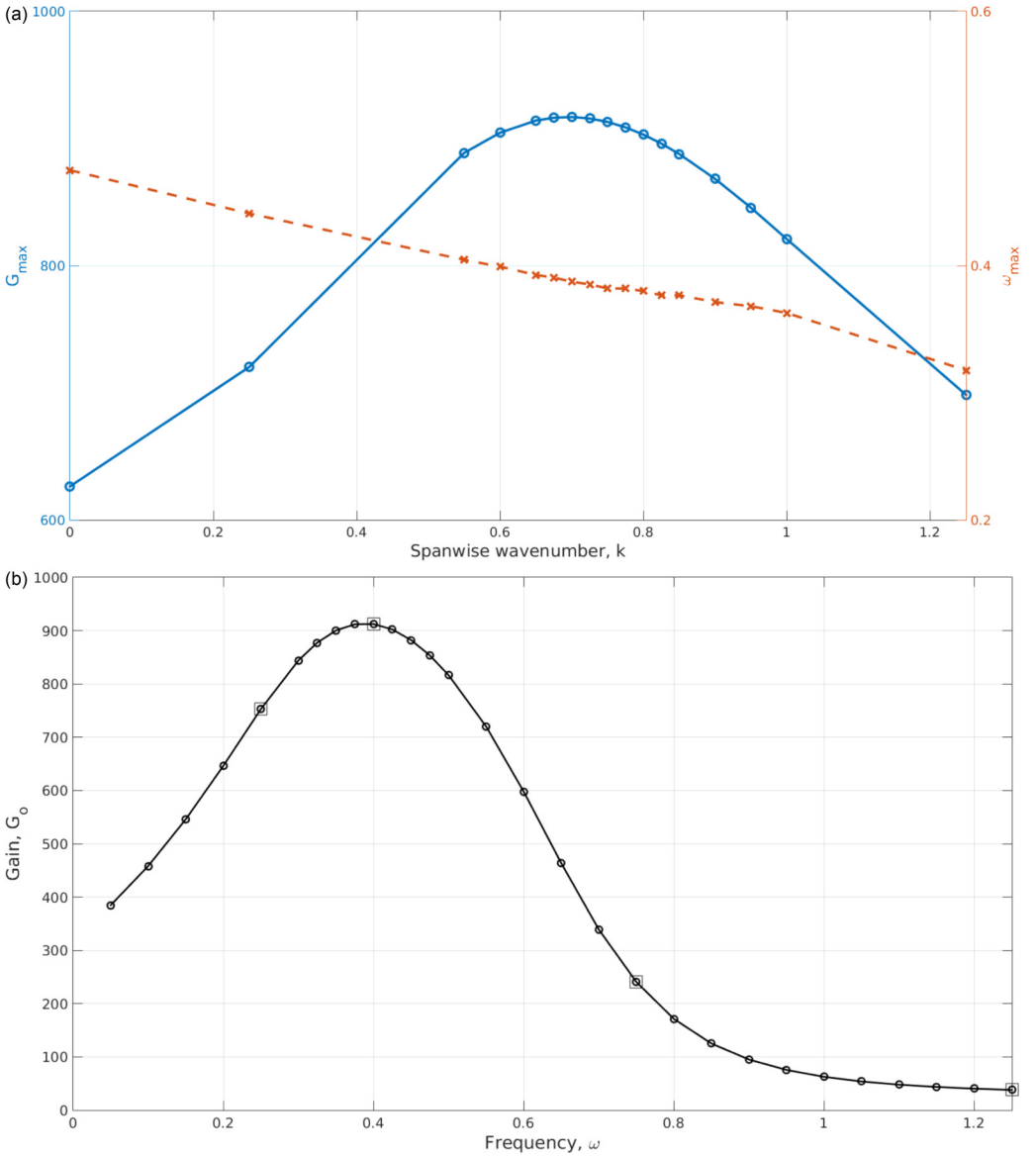

FIG. 5. (a) The maximum gain, G_{max} (solid), and the frequency at which this occurs, ω_{max} (dashed), as a function of the spanwise wave number k. (b) The optimal gain curve for forcing with $k = 0.7$.

which it occurs $\omega_{max}(k)$ vary with the spanwise wave number k. For each value of the spanwise wave number k, we find (ω_{max}, G_{max}) using a secant method. We observe that the maximum gain occurs for a forcing with a spanwise wave number $k = 0.7$. This corresponds to a spanwise wavelength of $L_z = 2\pi/k = 8.97$ cavity depths. The frequency at which the maximum gain occurs decreases nearly linearly with increasing spanwise wave number. This suggests that the structure most amplified by harmonic forcing shows strong spanwise shear layers which mathematically manifest themselves in a constant spanwise phase velocity, and thus explains the observed linear dependence of the peak frequency on the spanwise wave number. A phase locking of the most amplified structures across different spanwise wave numbers would corroborate this hypothesis.

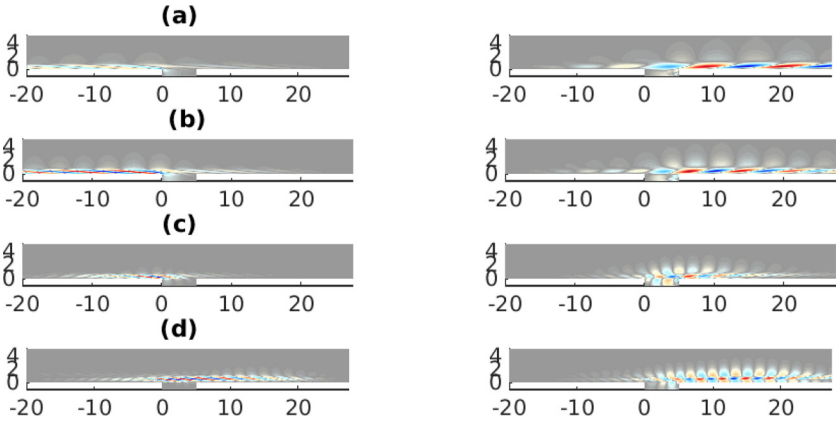

FIG. 6. The real component of the streamwise velocity of the optimal forcing (left) and response (right) for a range of frequencies for forcing with $k = 0.7$. (a) $\omega = 0.25$, (b) $\omega = 0.4$, (c) $\omega = 0.75$, and (d) $\omega = 1.25$.

The optimal gain and forcing are displayed in Fig. 6(b). The optimal forcing consists of flow structures in the boundary layer, as before tilted against the mean shear. The optimal response consists of flow structures in the boundary layer tilted in the direction of the mean shear; it corresponds to oblique waves developing in the boundary layer. The optimal response at $\omega = 0.25$ and $\omega = 0.75$ behaves in a manner similar to that observed for two-dimensional forcing. At $\omega = 1.25$, however, the optimal forcing and response are now localized in the boundary layer rather than the free stream. These correspond to an amplification of perturbations in the separated shear layer above the cavity to produce a response in the boundary layer downstream of the cavity. Structures corresponding to the amplification of vortical free-stream disturbances could also be found, but now correspond to suboptimal singular values.

D. Effect of Reynolds number

Next we consider the effect of the Reynolds number on the optimal response to two-dimensional forcing. The results are shown in Fig. 7(a) together with the local temporal growth rate (b) for increasing Reynolds numbers. For $\mathrm{Re} = 1000$ there exists only one pocket of convective instability in the flow, $0 < x < 6.1$.

For $\mathrm{Re} = 1300$, this pocket is larger, $0 < x < 6.7$, and a second pocket of convective instability exists downstream of the cavity, where the boundary layer is locally unstable to Tollmien-Schlichting (TS) waves, $x > 21$. To consider the effect of this second pocket of instability, we apply a masking function to the norm matrix $\mathbf{Q}$; more specifically, we focus on the contribution of the region $x > X_m$. This is shown in Fig. 8. For both cases, we find that, at low frequencies, the region $x > X_m$

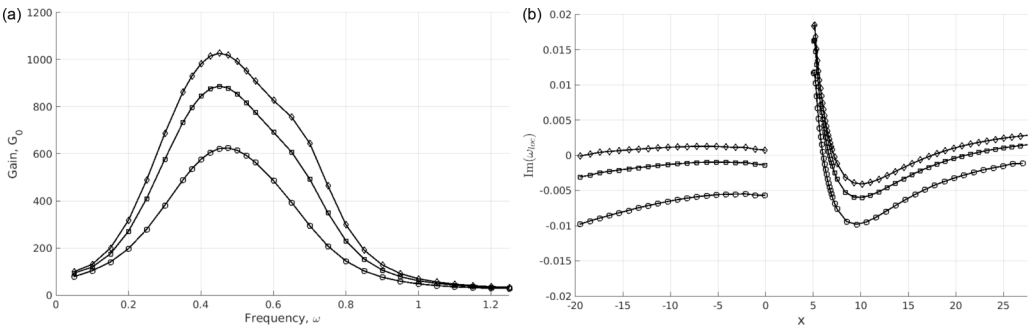

FIG. 7. (a) Optimal gain curves for two-dimensional forcing, and (b) the local temporal growth rate curves for $\mathrm{Re} = 1000$ (circles), $\mathrm{Re} = 1300$ (squares), and $\mathrm{Re} = 1500$ (diamonds).

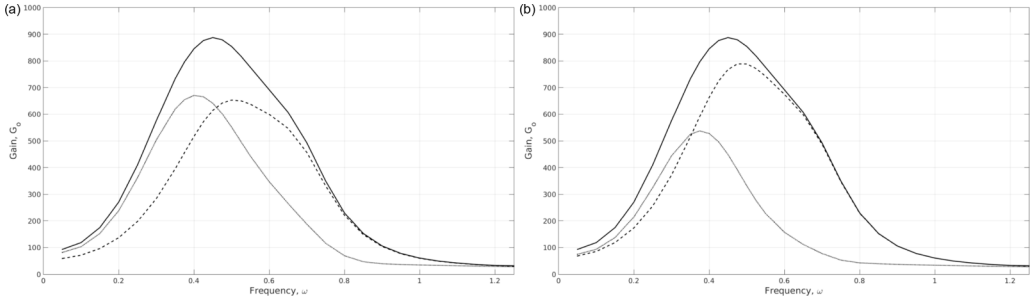

FIG. 8. The optimal gain curves obtained by applying a masking function to compare the contribution of the region $x < X_m$ (dashed) and $x > X_m$ (dotted) to the overall gain (solid) for (a) $X_m = 10$ and (b) $X_m = 15$ for a cavity with $L = 5$ and $D = 1$ at $\mathrm{Re} = 1300$.

experiences larger gain than the region $x < X_m$. This effect is related to the downstream pocket of instability associated with the TS-instability mechanism. The high-frequency behavior is, once again, dominated by the region $x < X_m$ representing the influence of the cavity.

For even larger Reynolds number, $\mathrm{Re} = 1500$, the flow is locally unstable from the inlet to the outlet except for a small region downstream of the cavity. From Fig. 7(a), we note that the frequency that is optimally amplified changes very little as the Reynolds number increases. This implies that the pocket of instability associated with the cavity has a markedly stronger influence on the amplification properties of the flow than the TS mechanism.

We observe a similar trend for the response to three-dimensional forcing (not shown here). The frequency and spanwise wave number that are optimally amplified change very little as the Reynolds number increases. We expect this trend to carry on for higher Reynolds numbers. These results suggest that even under conditions where the boundary layer is unstable, the amplification associated with the cavity will have a dominant influence on the dynamics.

E. Relation to global stability

The flow first becomes globally unstable to a centrifugal cavity mode with $k \approx 5$ at $\mathrm{Re} \approx 1750$. The structure of this unstable mode is different from the optimal responses seen in Fig. 6. This establishes that the behavior of the flow as a (globally unstable) amplifier is independent of the behavior of the flow as a (globally stable) oscillator at higher Reynolds numbers. The flow displays a clear selection principle for a preferred frequency and spanwise wavelength. Moreover, the amplification mechanism due to harmonic forcing is not linked to a resonance with a particular eigenmode, as can be seen from the eigenvalue spectra plots in Fig. 9.

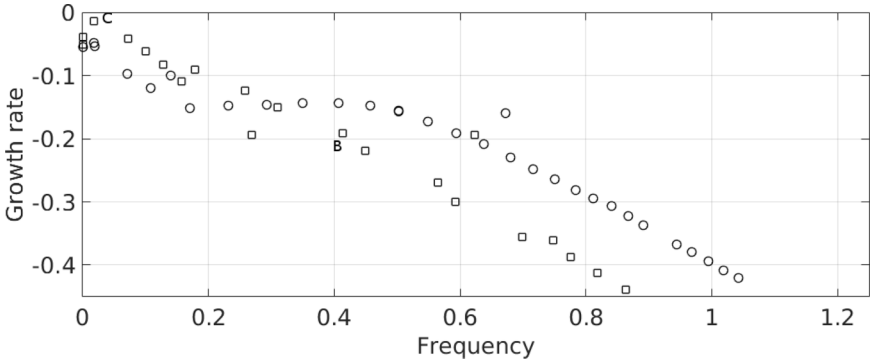

FIG. 9. The least stable part of the eigenvalue spectrum for two-dimensional ($k = 0$, circles) and three-dimensional ($k = 0.7$, squares) perturbations to the steady flow in Fig. 1.

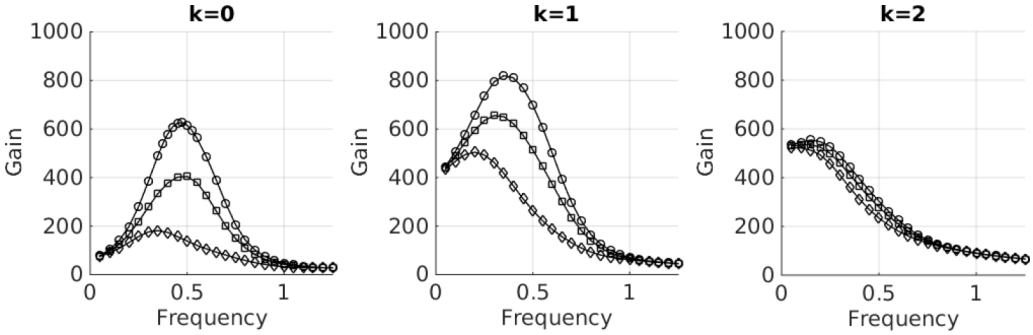

FIG. 10. Optimal gain vs frequency for cavities with $D = 1$ and $L = 5$ (circles), $L = 4$ (squares), and $L = 2$ (diamonds) at $\mathrm{Re} = 1000$.

F. Effect of cavity geometry

We carry out a parametric study to investigate the effect of cavity geometry on the frequency and spanwise wavelength of the most amplified mode. Figures 10 and 11 show the effect of varying the length L and depth D of the cavity on the optimal gain curves for a range of spanwise wave numbers $k = 0,1,2$. As expected, a shorter or more shallow cavity has a lower maximum gain. The difference between the gain curves is significant for $k = 0$ and $k = 1$, but little for $k = 2$. This suggests that the response to forcing with higher spanwise wave numbers becomes less sensitive to cavity geometry; only forcing that impacts the shallow cavity head on can extract energy from the base flow and result in significant amplification over a limited frequency range. Figure 12 summarizes how the gain, frequency, and spanwise wave number of the most amplified response vary with cavity length. We find that longer cavities experience a larger optimal gain and preferentially select and amplify a higher frequency and a lower spanwise wave number (larger spanwise wavelength).

IV. FREQUENCY SELECTION MECHANISM

We can understand more about the frequency selection mechanism using a perturbation or sensitivity analysis of the frequency response or the resolvent norm. Similar to a structural sensitivity analysis of the stability [18], which identifies the regions in the flow where self-amplification (i.e., the product of instability and receptivity) is maximal, a similar analysis for amplifier flows will reveal the regions in the flow where a frequency-selective response mechanism is most prevalent.

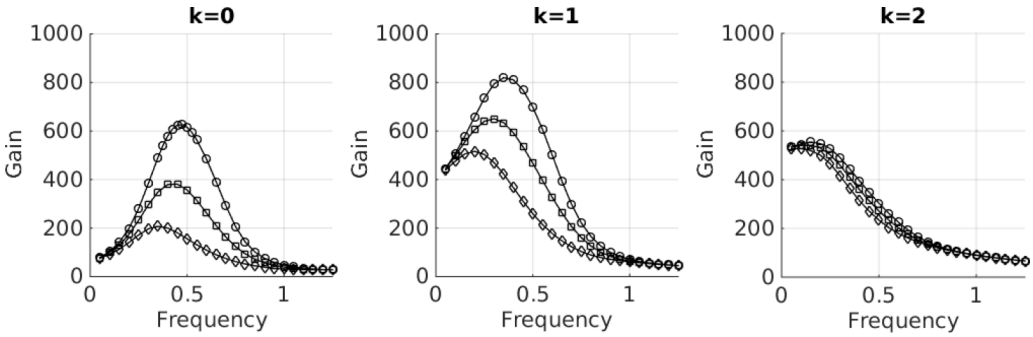

FIG. 11. Optimal gain vs frequency for cavities with $L = 5$ and $D = 1$ (circles), $D = 0.8$ (squares), and $D = 0.5$ (diamonds) at $\mathrm{Re} = 1000$.

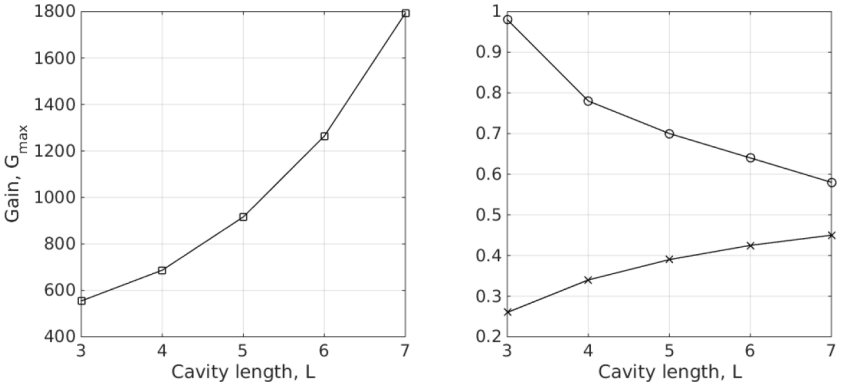

FIG. 12. Gain (squares), frequency (crosses), and spanwise wave number (circles) of the most amplified response for a cavity with $D = 1$ at $\mathrm{Re} = 1000$.

A. Formulation

We consider the effect of small perturbations to the linearized operator $\mathbf{L}$ on the optimal gain G. Mathematically, we carry out a perturbation analysis for the eigenvalue problem (5) that we solve to obtain the optimal gain and the optimal forcing. The perturbed problem reads

$$\mathbf{R}^H\mathbf{Q}\mathbf{R}\,\delta\hat{\mathbf{f}} + (\delta\mathbf{R})^H\mathbf{Q}\mathbf{R}\,\hat{\mathbf{f}} + \mathbf{R}^H\mathbf{Q}(\delta\mathbf{R})\,\hat{\mathbf{f}} = G^2\mathbf{Q}_\mathbf{f}\,\delta\hat{\mathbf{f}} + 2G(\delta G)\mathbf{Q}_\mathbf{f}\,\hat{\mathbf{f}}. \tag{6}$$

Collecting terms containing $\delta\hat{\mathbf{f}}$, we obtain $(G^2\mathbf{Q}_\mathbf{f} - \mathbf{R}^H\mathbf{Q}\mathbf{R})\,\delta\hat{\mathbf{f}} = 0$ from the original unperturbed problem (5). This subsequently simplifies the problem to

$$(\delta\mathbf{R})^H\mathbf{Q}\mathbf{R}\,\hat{\mathbf{f}} + \mathbf{R}^H\mathbf{Q}(\delta\mathbf{R})\,\hat{\mathbf{f}} = 2G(\delta G)\mathbf{Q}_\mathbf{f}\,\hat{\mathbf{f}}. \tag{7}$$

Premultiplying the above expression by $\hat{\mathbf{f}}^H$, we obtain

$$\hat{\mathbf{f}}^H(\delta\mathbf{R})^H\mathbf{Q}\mathbf{R}\,\hat{\mathbf{f}} + \hat{\mathbf{f}}^H\mathbf{R}^H\mathbf{Q}(\delta\mathbf{R})\,\hat{\mathbf{f}} = 2G(\delta G)\,\hat{\mathbf{f}}^H\mathbf{Q}_\mathbf{f}\,\hat{\mathbf{f}}. \tag{8}$$

The term on the right-hand side provides a normalization condition for the forcing. We normalize the forcing such that $\hat{\mathbf{f}}^H\mathbf{Q}_\mathbf{f}\,\hat{\mathbf{f}} = 1$. The two terms on the left-hand side are conjugates. We can thus rewrite the expression above as follows

$$G(\delta G) = \mathrm{Re}(\hat{\mathbf{f}}^H\mathbf{R}^H\mathbf{Q}(\delta\mathbf{R})\,\hat{\mathbf{f}}), \tag{9}$$

which can further be simplified, using the relation $\mathbf{R}\hat{\mathbf{f}} = G\hat{\mathbf{q}}$, to arrive at

$$\delta G = \mathrm{Re}(\hat{\mathbf{q}}^H\mathbf{Q}(\delta\mathbf{R})\,\hat{\mathbf{f}}). \tag{10}$$

What remains to be established is a relation between changes in $\mathbf{L}$ and associated changes in the resolvent $\mathbf{R} \equiv (\mathbf{L} + \mathrm{i}\omega\mathbf{B})^{-1}\mathbf{B}_\mathbf{f}\mathbf{P}$. The perturbation to an inverse matrix is given by $\delta(\mathbf{M}^{-1}) = -\mathbf{M}^{-1}(\delta\mathbf{M})\mathbf{M}^{-1}$. If we write $\mathbf{A} \equiv (\mathbf{L} + \mathrm{i}\omega\mathbf{B})^{-1}$ for convenience, we can express $\delta\mathbf{R}$ in terms of $\delta\mathbf{L}$ as

$$\delta\mathbf{R} = -\mathbf{A}(\delta\mathbf{L})\mathbf{A}\mathbf{B}_\mathbf{f}\mathbf{P}. \tag{11}$$

Substituting this expression into (10), we obtain

$$\begin{aligned} -\delta G &= \mathrm{Re}(\hat{\mathbf{q}}^H\mathbf{Q}\mathbf{A}(\delta\mathbf{L})\mathbf{A}\mathbf{B}_\mathbf{f}\mathbf{P}\,\hat{\mathbf{f}}), \\ -\frac{\delta G}{G} &= \mathrm{Re}(\hat{\mathbf{q}}^H\mathbf{Q}\mathbf{A}(\delta\mathbf{L})\,\hat{\mathbf{q}}), \\ -\frac{\delta G}{G^2} &= \mathrm{Re}((\mathbf{B}_\mathbf{f}\mathbf{P}\hat{\mathbf{f}})^H\mathbf{A}^H\mathbf{Q}\mathbf{A}(\delta\mathbf{L})\hat{\mathbf{q}}). \end{aligned} \tag{12}$$

We are interested in the sensitivity of the optimal gain G to small localized changes in the linear governing equations such that $\delta G = \langle \nabla_{\mathbf{L}} G, \delta \mathbf{L} \rangle$. Following Giannetti and Luchini [18] [Eq. (8.4)], the perturbation of a particular component of the linearized operator can be captured by the product of the corresponding components of the forcing and response vectors. Equivalently, by introducing a δ function to localize the perturbation, we deduce that the structural sensitivity is equivalent to the dyadic product of the optimal forcing and the velocity response, i.e.,

$$\nabla_{\mathbf{L}} G = S_{ij} = G^2 \mathrm{Re}(\hat{f}_i \hat{u}_j^*). \tag{13}$$

In this expression the subscripts $_{i,j}$ indicate the ith or jth component of the forcing or response. This expression is related to the sensitivity of the optimal gain to base-flow modifications, as introduced in Ref. [19], where $\nabla_{\bar{u}_i} G = G^2 \mathrm{Re}(\hat{u}_j^* \partial_j \hat{f}_i - \hat{f}_j \partial_i \hat{u}_j^*)$. Base-flow modifications are one specific way of perturbing the governing equations and can lead to noticeable changes in the optimal gain. We consider the effect of more general perturbations to the governing equations; in particular, we seek to identify the regions and mechanisms that drive the optimal frequency response. A region of high sensitivity is a region where small changes have a large effect on the gain; consequently, this region is influential in the linear nonmodal amplification of disturbances by harmonic excitation.

For three-dimensional forcing, the sensitivity tensor S_{ij} consists of nine entries, each describing how the ith component of forcing drives the jth component of the response. Analyzing the individual components of S_{ij} enables us to identify not only the regions of our flow domain that are influential, but also the component-wise interactions that are responsible for the optimal response to harmonic forcing. We do not suggest that these components be individually perturbed—physically, this would be infeasible. Rather, we consider this to be a useful mathematical formalism to identify their relative contribution to the gain.

B. Validation: Application to parallel Poiseuille flow

Before applying the above concept of structural sensitivity of the frequency response to the case of shallow cavities, we illustrate and validate this idea by considering the optimal response of plane Poiseuille flow at $\mathrm{Re} = 2000$ to steady and harmonic forcing. From previous studies [20–22], we know that the lift-up mechanism is responsible for the largest gain of steady streamwise vortices to produce streaks. This involves energy transfer from the cross-stream and spanwise components to the streamwise components of velocity. The Orr mechanism also acts to amplify boundary-layer disturbances slanted against the mean shear to produce TS waves. This involves energy transfer within the streamwise and/or spanwise components only.

We find that the largest gain is obtained for steady forcing with a spanwise wave number $k = 1.62$. The optimal forcing takes the form of steady streamwise vortices, with a large spanwise velocity near the walls and large cross-stream velocities near the centerline. The forcing is constant in the streamwise direction. The corresponding optimal response takes the form of steady, streamwise-independent streaks with large streamwise velocities near the wall. The associated lift-up mechanism is responsible for the nonmodal amplification [20,22]. In Fig. 13, we plot the nine components of the sensitivity tensor for the optimal response and find that the gain is most sensitive to the spanwise component of forcing, producing a streamwise response. This observation is related to the energy transfer from the spanwise component of the vortical motion to the streamwise velocity of the streak. It is interesting to note that the gain is not sensitive to the cross-stream components of forcing as we would have expected from previous studies [20–22]. This is because the cross-stream components of the forcing have large magnitudes far from the wall, whereas the optimal response has large magnitudes near the wall. This spatial separation implies that the cross-stream components are far less efficient at amplifying structures near the walls and thus have a smaller effect on the gain than the spanwise components of the forcing (which have large magnitudes near the wall).

We find that large gains are also obtained for three-dimensional harmonic forcing. We consider the case with wave numbers $\alpha = 1$ and $k = 1$. For this set of parameters, the largest gain is obtained for forcing with a frequency of $\omega = 0.38$. The optimal forcing takes the form of near-wall structures with

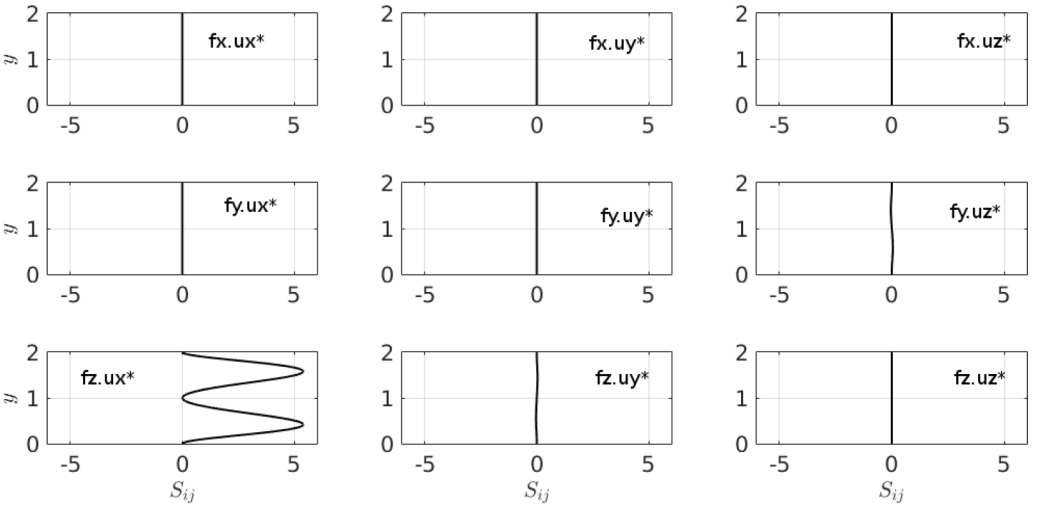

FIG. 13. The components of the sensitivity tensor $S_{ij} = \mathrm{Re}(\hat{\mathbf{f}}_i \hat{\mathbf{u}}_j^*)$ of the most amplified response due to the lift-up mechanism for plane Poiseuille flow at $\mathrm{Re} = 2000$ with $\alpha = 0$ and $k = 1.62$.

large streamwise and spanwise components aligned *against* the mean shear. The optimal response takes the form of near-wall structures also with large streamwise and spanwise components slanted in the direction of the mean shear. This response is similar to an oblique Tollmien-Schlichting wave. The Orr mechanism is responsible for the nonmodal amplification [20]. Figure 14 shows the components of the sensitivity tensor for this response. We find that the gain is most sensitive to the streamwise and spanwise components of the forcing and response. Since $\alpha = k$ here, the gain is equally sensitive to the streamwise and spanwise components. For different values, we would expect the gain to be more sensitive to the component of the dominant direction.

These findings should be compared to the results from an input-output analysis for channel flow [21], where the effect of the different components of forcing on the different components of the

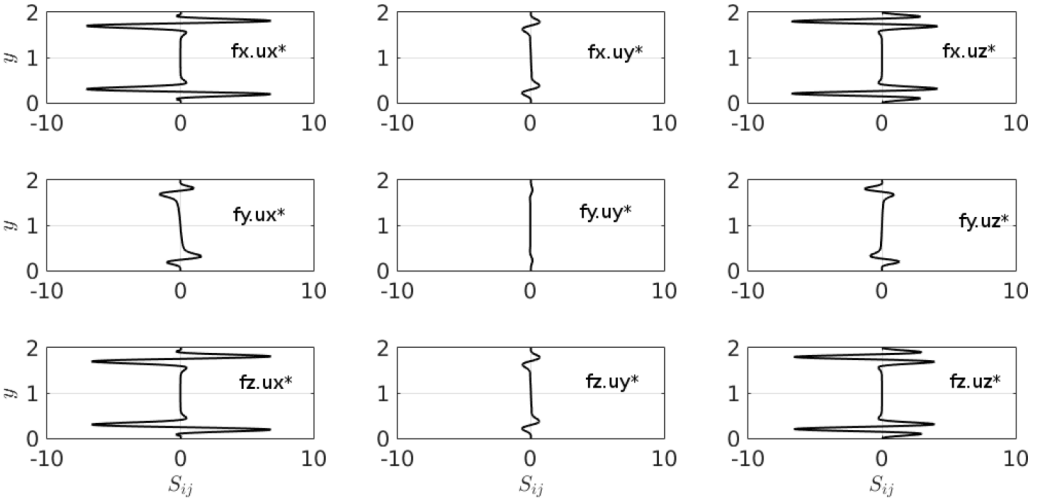

FIG. 14. The components of the sensitivity tensor $S_{ij} = \mathrm{Re}(\hat{\mathbf{f}}_i \hat{\mathbf{u}}_j^*)$ of the most amplified response at $\omega = 0.38$ due to the Orr mechanism for plane Poiseuille flow at $\mathrm{Re} = 2000$ with $\alpha = 1$ and $k = 1$.

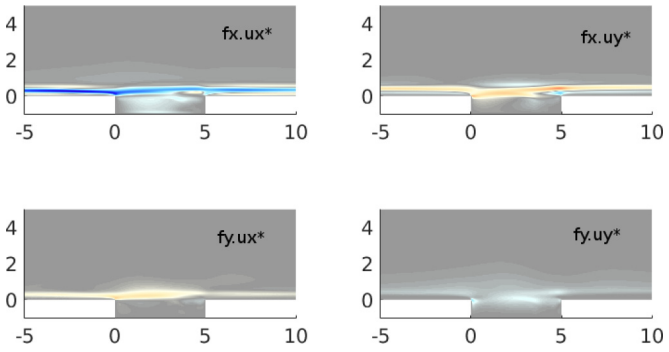

FIG. 15. The components of the sensitivity tensor $S_{ij} = \mathrm{Re}(\hat{\mathbf{f}}_i \hat{\mathbf{u}}_j^*)$ of the most amplified response to two-dimensional forcing shown in Fig. 3(b).

response have been deduced from the transfer functions of the nine forcing-response combinations. Spanwise and cross-stream components of forcing have been found to have the largest influence, while the largest response is found in the streamwise components. Our results on the sensitivity of the frequency response for plane channel flow corroborate these findings.

C. Application to flow over a shallow cavity

We consider the structural sensitivity of the optimal response to two-dimensional and three-dimensional forcing. In Figs. 15 and 16, we display the components of the sensitivity tensor for the most amplified modes. The highest magnitudes are observed in the components involving the streamwise and spanwise components, in the regions of the boundary layer upstream and downstream of the cavity. This fact highlights the importance of convective non-normality in driving the response. The small influence of the cross-stream components suggests that the lift-up mechanism is not influential in the amplification process. Furthermore, we do not see any footprint or involvement of the flow inside the cavity on the optimal frequency response.

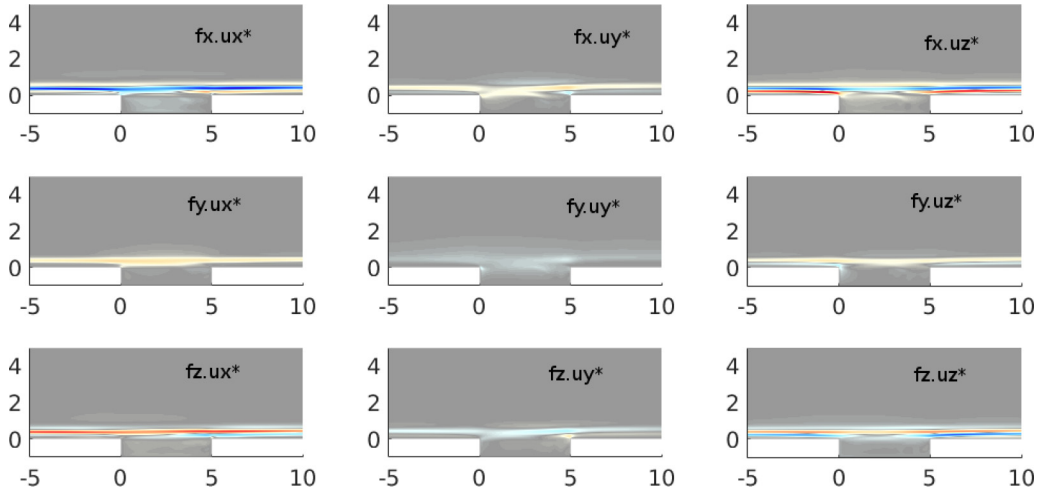

FIG. 16. The components of the sensitivity tensor $S_{ij} = \mathrm{Re}(\hat{\mathbf{f}}_i \hat{\mathbf{u}}_j^*)$ of the most amplified response shown in Fig. 6(b).

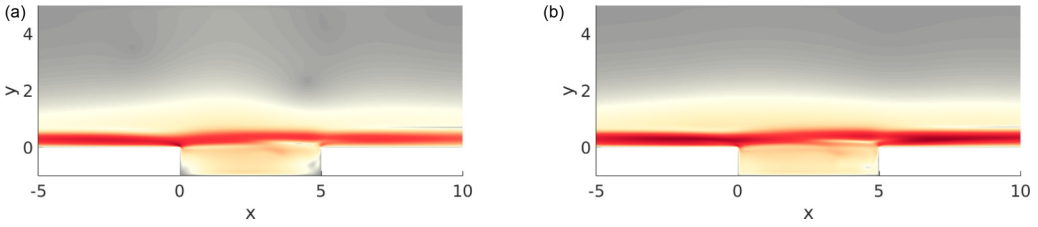

FIG. 17. The Frobenius norm of the structural sensitivity tensors for the optimal response to (a) two-dimensional and (b) three-dimensional harmonic forcing.

We can identify the region of the flow that drives the response more clearly by taking a suitable norm of the sensitivity tensors. To this end, Fig. 17 depicts the Frobenius norm of the sensitivity tensors for the optimal response to two-dimensional and three-dimensional harmonic forcing. For two-dimensional forcing, the sensitivity is largest at the upstream edge of the cavity. This agrees perfectly with the local stability analysis, which identifies the upstream edge of the cavity as the stable/unstable boundary. There is a clear relationship between the global optimal frequency response and the local stability analysis for two-dimensional forcing.

In contrast, for three-dimensional forcing, the sensitivity is largest in the regions just upstream and downstream of the cavity. As a consequence, these regions play a dominant role in the selection of the optimal response to harmonic forcing. The same figure furthermore suggests that, for the amplification of disturbances in the flow over a shallow cavity, the changes induced by the cavity in the boundary layer directly upstream and downstream are more important than the flow in the cavity itself.

We can understand this better in terms of competition between the different dynamics and time scales associated with the flow inside the cavity and the flow outside the cavity. The slow recirculating flow inside the cavity is associated with a centrifugal instability mechanism [6] that leads to a low-frequency global instability. The boundary layer developing outside the cavity is associated with the nonmodal Orr mechanism that leads to strong amplification of disturbances with a smaller wavelength.

In response to harmonic forcing, these instability mechanisms can produce a response either through resonance with a particular mode, or pseudoresonance. We can compare the potential strength of these responses. We choose two modes from the global spectrum shown in Fig. 9 that represent a response in the cavity (labeled C, with an eigenvalue $-0.01 + 0.02\mathrm{i}$), and a response in the boundary layer downstream (labeled B, with an eigenvalue $-0.19 + 0.43\mathrm{i}$). We also calculate the associated adjoint global modes. We normalize the modes to have unit energy norm so that $\hat{\mathbf{q}}^H \mathbf{Q} \hat{\mathbf{q}} = \hat{\mathbf{q}}^{+H} \mathbf{Q} \hat{\mathbf{q}}^+ = 1$.

The potential strength of a pseudoresonance between the two modes can be quantified by the inner product between them, $\hat{\mathbf{q}}_C^H \mathbf{Q} \hat{\mathbf{q}}_B$. We obtain a value of 0.02, which suggests that the response in the cavity and the response in the boundary layer mode are almost orthogonal to each other. There is thus very little potential for interaction between these two modes.

The potential for amplification of the forcing due to non-normality can be quantified by the inverse of the inner product between the mode and its associated adjoint $(\hat{\mathbf{q}}^H \mathbf{Q} \hat{\mathbf{q}}^+)^{-1}$ [8]. For the cavity mode, we obtain a value of 1.82, whereas for the boundary layer mode, we obtain a value of 3.48×10^7.

The consequence of these two factors is that perturbations in the boundary layer experience much stronger amplification due to the Orr mechanism in comparison to perturbations in the cavity over a range of forcing frequencies. In the regions immediately downstream and upstream of the cavity, the Orr mechanism is stronger due to the "non-Blasiusness" of the boundary layer profiles. These regions therefore play a dominant role in the response of the flow.

V. SUMMARY AND CONCLUSIONS

In this study, we have analyzed the linear dynamics of the laminar flow over a shallow cavity. The flow configuration is chosen such that the boundary layer is locally stable at the inlet and outlet of the computational domain. The flow is characterized by a pocket of local convective instability extending from the upstream edge of the cavity to some distance downstream of the cavity. Nonetheless, the flow is globally stable.

We have determined the linear frequency response for two-dimensional and three-dimensional harmonic forcing and have identified the spatial structure of the optimal forcing and response corresponding to the largest possible gain. We find that the flow exhibits substantial optimal gains for both two-dimensional and three-dimensional forcing, but the largest gain is obtained for three-dimensional forcing. The most effective forcing takes the form of streamwise-elongated flow structures in the boundary layer upstream of the cavity, inducing a response that takes the form of an oblique wave (reminiscent of an oblique Tollmien-Schlichting wave). These structures suggest that the Orr mechanism plays an important role in the nonmodal amplification of the forcing. Moreover, we establish that the optimal response is not linked to resonance with any particular eigenvalue and that it is distinct from the globally unstable cavity mode that develops at higher Reynolds numbers.

While the gain to harmonic forcing increases as the Reynolds number is increased, the frequency and spanwise wave number where this amplification is observed shows only a weak dependence on the Reynolds number. This observation suggests a robust frequency and structure selection mechanism that is active across a range of Reynolds numbers. Locating the spatial domains that are most sensitive to harmonic forcing revealed that high-frequency structures are most effectively influenced by the cavity, while low-frequency structures are best triggered further downstream of the cavity. For selecting the most amplified frequency, however, the cavity plays an important role.

We have investigated the effect of cavity geometry on the optimal frequency response. This reveals that the optimal gain curves for forcing at higher spanwise wave numbers is less affected as the cavity's length and depth are varied. The optimal response for longer cavities has a higher frequency and a larger spanwise wavelength.

Finally, we have introduced a sensitivity analysis that captures the effect of small changes in the linear governing equations on the optimal gain. By overlapping the optimal forcing and response, similar to structural sensitivity analyses of globally unstable flows, we identify the regions of highest sensitivity in the flow; these correspond to regions that drive the frequency response and identify regions in the flow that are responsible for the observed amplification of preferred frequencies. For the shallow cavity, the regions upstream and downstream of the cavity exhibit the highest sensitivity and are most involved in the selection process of the most-amplified frequencies. This suggests that the optimal response and the shape of the flow's transfer function are driven by the modification that the cavity exerts on the boundary layer (in particular, immediately upstream and downstream of the cavity) rather than by the flow in the cavity itself.

Besides the analytic aspect of our investigation, this study has implications for the design of active or passive control strategies that aim to mitigate the amplification of particular frequencies

TABLE I. Domain size ($X_{\min}$, $X_{\max}$, $Y_{\max}$) and number of finite elements (n_{tri}) used in the calculations. The optimal gain $G_{\max}|_{k=0}$ and frequency ($\omega_{\max}|_{k=0}$) of the most amplified two-dimensional mode are listed for four different mesh configurations.

	$X_{\min}$	$X_{\max}$	$Y_{\max}$	n_{tri}	$G_{\max}\|_{k=0}$	$\omega_{\max}\|_{k=0}$
M_1	−20	27.5	5	214647	625	0.465
M_2	−20	27.5	7	306067	647	0.460
M_3	−25	32.5	5	233280	629	0.460
M_4	−20	27.5	5	321522	625	0.470

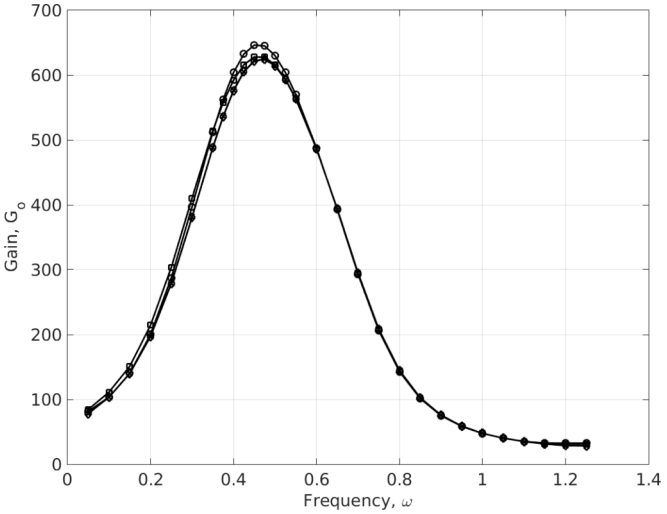

FIG. 18. The optimal gain curves for two-dimensional forcing, computed on four different meshes: M_1 (crosses), M_2 (circles), M_3 (squares), and M_4 (diamonds).

by surface irregularities, such as small gaps, dips, steps, protrusions, or other localized roughness elements. Our analysis provides guidance for an effective setup of actuator and sensor elements and suggests that manipulation of the regions immediately upstream and downstream of the irregularities is most appropriate for controlling roughness-induced flow responses.

ACKNOWLEDGMENTS

The authors acknowledge the support of the Engineering and Physical Sciences Research Council through Grant No. EP/I037946/1 and thank the referees for their insightful comments.

APPENDIX: NUMERICAL CONVERGENCE

We calculate the base flow and optimal frequency response to two-dimensional forcing on several different meshes in order to assess the reliability and convergence of the results. Table I compares the frequency and optimal gain while varying the number of degrees of freedom and domain size. The optimal gain curves are plotted in Fig. 18. Mesh M_1 is used throughout this study. Mesh M_2 has the same spatial resolution as M_1, but a larger value of $Y_{\max}$. Mesh M_3 has the same spatial resolution as M_1, but a larger value of $X_{\max}$. Mesh M_4 has 1.5 times the spatial resolution of M_1, but the domain size is the same. The results show a maximum discrepancy of less than 5% for the optimal gain and optimal frequency with respect to M_1. We conclude that mesh M_1 is sufficient to produce results that are grid independent.

[1] V. Theofilis, S. Hein, and U. Dallmann, On the origins of unsteadiness and three-dimensionality in a laminar separation bubble, Philos. Trans. R. Soc. London, Ser. A **358**, 3229 (2000).

[2] D. Barkley, M. Gomes, and R. Henderson, Three-dimensional instability in flow over a backward-facing step, J. Fluid Mech. **473**, 167 (2002).

[3] G. Bres and T. Colonius, Three-dimensional instabilities in compressible flow over open cavities, J. Fluid Mech. **599**, 309 (2008).

[4] J. de Vicente, J. Basley, F. Meseguer-Garrido, J. Soria, and V. Theofilis, Three-dimensional instabilities over a rectangular open cavity: From linear stability analysis to experimentation, J. Fluid. Mech. **748**, 189 (2014).
[5] F. Meseguer-Garrido, J. De Vicente, E. Valero, and V. Theofilis, On linear instability mechanisms in incompressible open cavity flow, J. Fluid Mech. **752**, 219 (2014).
[6] V. Citro, F. Giannetti, L. Brandt, and P. Luchini, Linear three-dimensional global and asymptotic stability analysis of incompressible open cavity flow, J. Fluid Mech. **768**, 113 (2015).
[7] D. Sipp and O. Marquet, Characterization of noise amplifiers with global singular modes: The case of the leading-edge flat plate boundary layer, Theor. Comput. Fluid Dyn. **27**, 617 (2013).
[8] J.-M. Chomaz, Global instabilities in spatially developing flows: Non-normality and nonlinearity, Annu. Rev. Fluid Mech. **37**, 357 (2005).
[9] P. Schmid, Nonmodal stability theory, Annu. Rev. Fluid Mech. **39**, 129 (2007).
[10] E. Åkervik, U. Ehrenstein, F. Gallaire, and D. Henningson, Global two-dimensional stability measures of the flat plate boundary-layer flow, Eur. J. Mech. B/Fluids **27**, 501 (2008).
[11] A. Monokrousos, E. Åkervik, L. Brandt, and D. Henningson, Global three-dimensional optimal disturbances in the Blasius boundary-layer flow using time-steppers, J. Fluid Mech. **650**, 181 (2010).
[12] F. Alizard, S. Cherubini, and J.-C. Robinet, Sensitivity and optimal forcing response in separated boundary layer flows, Phys. Fluids **21**, 064108 (2009).
[13] E. Boujo, U. Ehrenstein, and F. Gallaire, Open-loop control of noise amplification in a separated boundary layer flow, Phys. Fluids **25**, 124106 (2013).
[14] G. Dergham, D. Sipp, and J.-C. Robinet, Stochastic dynamics and model reduction of amplifier flows: The backward facing step flow, J. Fluid Mech. **719**, 406 (2013).
[15] X. Garnaud, L. Lesshafft, P. Schmid, and P. Huerre, The preferred mode of incompressible jets: Linear frequency response analysis, J. Fluid Mech. **716**, 189 (2013).
[16] S. Cerqueira and D. Sipp, Eigenvalue sensitivity, singular values, and discrete frequency selection mechanism in noise amplifiers: The case of flow induced by radial wall injection, J. Fluid Mech. **757**, 770 (2014).
[17] D. Rodriguez, E. Gennaro, and M. Juniper, The two classes of primary modal instability in laminar separation bubbles, J. Fluid Mech. **734**, R4 (2013).
[18] F. Giannetti and P. Luchini, Structural sensitivity of the first instability of the cylinder wake, J. Fluid Mech. **581**, 167 (2007).
[19] L. Brandt, D. Sipp, J. Pralits, and O. Marquet, Effect of base-flow variation in noise amplifiers: The flat-plate boundary layer, J. Fluid Mech. **687**, 503 (2011).
[20] K. Butler and B. Farrell, Three-dimensional optimal perturbations in viscous shear flow, Phys. Fluids **4**, 1637 (1992).
[21] M. Jovanovic and B. Bamieh, Componentwise energy amplification in channel flows, J. Fluid Mech. **534**, 145 (2005).
[22] P. Schmid and D. Henningson, *Stability and Transition in Shear Flows* (Springer-Verlag, New York, 2001).